






Temperature and magnetic field dependent Raman study of electron-phonon interactions in thin films of Bi₂Se₃ and Bi₂Te₃ nanoflakes

Sören Buchenau ^{1,*}, Sarah Scheitz ¹, Astha Sethi,² John E. Slimak,² Tomke Eva Glier ¹, Pranab Kumar Das ³, Torben Dankwort,⁴ Lewis Akinsinde,¹ Lorenz Kienle,⁴ Andriwo Rusydi,³ Clemens Ulrich ⁵, S. Lance Cooper,² and Michael Rübhausen¹

¹CFEL, University Hamburg, Luruper Chaussee 175, 22761 Hamburg, Germany

²Department of Physics and Materials Research Laboratory, University of Illinois, Urbana, Illinois 61801, USA

³Singapore Synchrotron Light Source, National University of Singapore, Singapore 117603, Singapore

⁴Institute for Materials Science, Kiel University, Kaiserstrasse 2, 24143 Kiel, Germany

⁵School of Physics, The University of New South Wales, New South Wales 2052, Sydney, Australia



(Received 8 October 2019; accepted 26 May 2020; published 22 June 2020)

We have investigated two-dimensional nanostructures of the topological insulators Bi₂Se₃ and Bi₂Te₃ by means of temperature and magnetic field dependent Raman spectroscopy. The surface contribution of our samples was increased by using thin films of dropcasted nanoflakes with the aim of enhancing their topological properties. Raman spectroscopy provides a contact-free method to investigate the behavior of topological properties with temperature and magnetic fields at lower dimensions. The temperature dependent Raman study reveals anharmonic phonon behavior for Bi₂Te₃ indicative of a two-phonon relaxation mechanism in this material. Contrary to this, Bi₂Se₃ shows clear deviations from a two-phonon anharmonic decay model at temperatures below 120 K exhibiting a hardening and broadening, especially of the A_{1g}² mode. Similarly, the magnetic field dependent self-energy effects are only observed for the A_{1g}² mode of Bi₂Se₃, showing a broadening and hardening with increasing field. We interpret our results in terms of corrections to the phonon self-energy for Bi₂Se₃ at temperatures below 120 K and magnetic fields above 4 T due to electron-hole pair excitations associated with the conducting surface states. The phonon renormalization with increasing magnetic field is explained by a gap opening in the Dirac cone that enables phonon coupling to the changing electric susceptibility.

DOI: [10.1103/PhysRevB.101.245431](https://doi.org/10.1103/PhysRevB.101.245431)

I. INTRODUCTION

Topological insulators (TIs) are a new class of materials, which are insulating in the bulk and host conducting surface states (CSSs) at the interface between the TI and conventional insulators [1]. The idea of topological states was strongly promoted during the aftermath of the discovery of the quantum Hall effect by von Klitzing [2], who identified specific quantized changes in the Hall conductance, which turn out to be topological quantum numbers. After several incremental steps, modern three-dimensional (3D) TIs were predicted in 2007 by Fu *et al.* [3]. The strong spin-orbit coupling leads, in specific materials, to a band inversion of two *p* bands [4], which is essential for the CSSs. In addition, the electron transport is characterized by spin-momentum locking and a linear dispersion relation, known as a Dirac cone, superimposed on the bulk bands [5]. Bi₂X₃ (X=Se, Te) belongs to the most frequently studied 3D TI with a single Dirac cone at the Γ point of the Brillouin zone [6,7] and bulk band gaps of 0.3 eV [8] and 0.1 eV [9] for Bi₂Se₃ and Bi₂Te₃, respectively.

To explicitly study the CSSs and reduce contributions from the bulk, we have examined dropcasted nanoflakes with high aspect ratios that lead to an increased surface contribution.

In order to evaluate the fundamental limit of the conductivity of electrons in the CSSs at lower dimensions, it is

important to study the electron-phonon interactions of these 2D materials [10,11].

A unique technique to study phononic and electronic properties of solids simultaneously is Raman scattering, which has been widely applied to investigate bulk samples and conventional 2D films of Bi₂Se₃ [12–15] and Bi₂Te₃ [14,16,17]. Bi₂Se₃ and Bi₂Te₃ are layered materials with a rhombohedral crystal structure that grow in multiples of so-called quintuple layers (QLs) consisting of alternating Bi and Se or Te layers, as depicted in Fig. 1(a) [18]. The primitive unit cell consists of five atoms, which results in 15 lattice dynamical modes that are classified in three acoustic and 12 optical modes. The optical modes are further grouped into four Raman-active modes with two modes each of A_{1g} and E_g symmetry and four infrared(IR)-active modes with two modes each of A_{1u} and E_u symmetry according to group theory [18]. Due to the inversion symmetry of the crystal structure, these phonon modes are exclusively either Raman or IR active [18]. Of the Raman-active phonons, the A_{1g} modes are out-of-plane vibrations, whereas the E_g modes vibrate in-plane.

Systematic temperature dependent Raman studies have been conducted before on Bi₂Se₃ single crystals [19,20] and nanoplates [21], and on Bi₂Te₃ thin films [22]. In this work, we report on a temperature and magnetic field dependent high-energy-resolution Raman study of thin films of individual Bi₂Se₃ and Bi₂Te₃ nanoflakes with average heights in the range of 8 and 14 QLs, respectively.

*Corresponding author: sbuchena@physnet.uni-hamburg.de

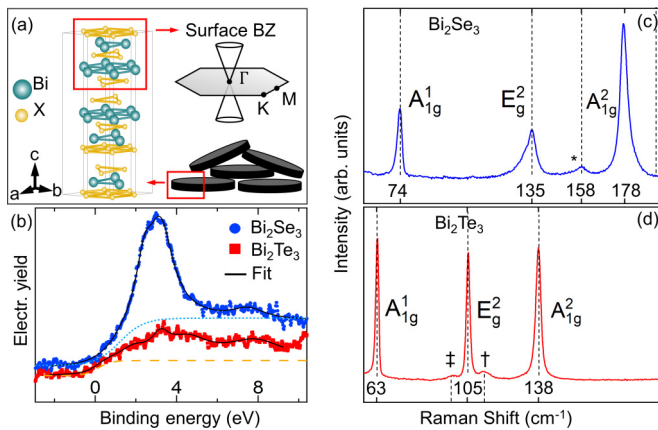


FIG. 1. (a) Schematic illustration of a thin film of Bi_2X_3 ($\text{X} = \text{Se, Te}$) nanoflakes. This configuration greatly enhances the amount of surface, which hosts massless Dirac electrons due to the linear Dirac cone at the Γ point [29], as shown in the surface Brillouin zone in the upper right corner. The figure further shows the crystal structure with blue spheres representing Bi atoms and yellow spheres representing either Se or Te atoms. (b) Valence-band emission spectra extracted from XPS spectra of both materials. The Fermi edge modeled by a step function shows a highly increased electron density for Bi_2Se_3 (light-blue, dotted graph) compared to Bi_2Te_3 (orange, dashed graph). (c),(d) Raman spectra at 3 K in $z(xx)\bar{z}$ geometry showing three labeled bulk modes for Bi_2Se_3 and Bi_2Te_3 , respectively. The asterisk, dagger, and double dagger mark Raman-forbidden infrared modes.

Magnetic field dependent Raman measurements are of utmost importance as they allow for investigations of the destruction of the CSSs by gapping of the Dirac cone induced by the presence of a magnetic field [1]. It was theoretically predicted that the CSSs are sensitive to the application of a magnetic field [23] and an opening of the Dirac cone has indeed been observed in magnetically doped TIs [24,25] or by exchange coupling TIs to magnetic insulators [26–28]. The tuning of the CSSs with an applied magnetic field is expected to display a spectroscopic signature, which is amplified due to the highly increased surface contributions of our nanoflakes. We therefore interpret our results by means of self-energy corrections of the phonons due to electron-phonon interactions.

II. EXPERIMENTAL PART

Figure 1(a) shows an illustration of strongly anisotropic nanoflakes. The Bi_2Se_3 nanoflakes were grown with the chemical polyol method following our earlier work [30]. The Bi_2Te_3 nanoflakes were synthesized using a slightly modified route according to Zhang *et al.* [31]. Details on the synthesis are presented in Ref. [30] and in the Supplemental Material [32]. The clean flakes were dropcasted on a Si substrate and the solvent evaporated. It should be noted that the structures are not damaged by these preparatory steps, as can be seen in Fig. S-2 of the Supplemental Material [32]. The required stoichiometry, single crystallinity, and morphology of both samples were confirmed using energy dispersive x-ray spectroscopy (EDX), x-ray photoelectron spectroscopy (XPS), transmission electron microscopy (TEM), selected area electron diffraction (SAED), and atomic

force microscopy (AFM). A detailed characterization of the nanoflakes can be found in the Supplemental Material [32].

The topological insulator Bi_2X_3 ($\text{X} = \text{Se, Te}$) features Dirac states at the interface with conventional insulators, but not at the interface of every QL [28]. It has furthermore been shown for Bi_2Se_3 , that the CSS wave functions hybridize below a critical flake thickness of 6 QLs, which results in a gap opening in the Dirac cone [33]. To investigate the intact CSSs, it is hence necessary to grow flakes of certain thicknesses and maintain enough space between dropcasted flakes to prevent hybridization of the CSSs from neighboring flake surfaces. With average heights of 8 and 14 QLs for our Bi_2Se_3 and Bi_2Te_3 flakes, respectively, we expect our samples to host unperturbed CSSs. In addition, our flakes were grown covered with the ligand polyvinylpyrrolidone (PVP) to facilitate a 2D growth. The PVP layers act as conventional insulators and thus provide sufficient spacing between neighboring flakes. It is known that the CSSs are robust against different kinds of adsorbates and are maintained even under ambient environmental conditions [24,34]. However, adsorbates are known to induce a band bending of the bulk bands near the surface due to charge accumulation [6,35]. This leads to the creation of additional surface quantum well states originating from the bulk bands coexisting next to the CSSs. Nonetheless, the CSSs stay intact, but are pushed deeper into the bulk separating them from the surface defects [36]. Thus, for volume scattering techniques, the CSSs stay detectable as Raman scattering is able to probe the whole volume including the deeper-lying CSSs, in contrast to surface sensitive techniques such as angle-resolved photoemission spectroscopy (ARPES). In fact, Raman scattering probes the complete thickness of a flake of about 10 nm. Therefore, probing a thin film of dropcasted nanoflakes is expected to contain a manifold of topologically nontrivial contributions, as illustrated in Fig. 1(a), making it easier to observe phenomena that have their origin in those exotic states.

We conducted Raman measurements on films of dropcasted nanoflakes using the 647.1 nm excitation line of a continuous-wave Kr^+ gas laser. The incident laser power was limited to 6.2 mW and focused on a 50- μm -diameter spot size to prevent laser induced heating or damage of the sample, which is shown in detail in the Supplemental Material [32]. The sample was mounted so that the incident light impinged on the flakes perpendicular to their surfaces. The scattered light from the sample was collected in a backscattering configuration, dispersed through a triple-stage spectrometer, and then detected with a liquid-nitrogen-cooled charged-coupled-device detector. The horizontal polarization of the incident light with regard to the setup was selected with a polarization rotator and the scattered light was analyzed by the triple-stage gratings of the spectrometer that is primarily sensitive to horizontally polarized light [37]. Our scattering configuration denoted in Porto notation is hence $z(xx)\bar{z}$ [38]. The samples were inserted into a continuous He-flow cryostat, which itself was horizontally mounted in the open bore of a superconducting magnet. This setup allowed for simultaneous temperature (3–295 K) and magnetic field (0–7 T) dependent measurements. Magnetic field dependent measurements were performed in Faraday geometry with the wave vector of the incident light \vec{q} parallel to the applied field \vec{H} .

III. RESULTS AND DISCUSSION

Figure 1(b) shows the valence-band spectra extracted from XPS measurements of the Bi_2Se_3 and Bi_2Te_3 films. The indicated Fermi edges modeled by step functions reveal, for Bi_2Se_3 , a highly increased electron density near the Fermi edge compared to Bi_2Te_3 . Differences in the two samples are also reflected in their phononic properties measured by Raman spectroscopy. The implication of the enhanced surface contribution of our flakes is already observable in the representative Raman spectra shown in Figs. 1(c) and 1(d). Next to the three identified bulk phonon modes that are in good agreement with previous experiments [18,39,40], additional IR-active modes at 158 cm^{-1} in Bi_2Se_3 and at 98 cm^{-1} and 113 cm^{-1} in Bi_2Te_3 are detected [14,15,41]. The IR-active modes become Raman active because of the breaking of the crystal's inversion symmetry at the surface of the nanoflakes [15]. This aspect is a direct manifestation of the enhanced surface-to-volume ratio of the dropcasted nanoflakes compared to the bulk material. The bulk material crystallizes in the D_{3d} space group with inversion symmetry, whereas the symmetry at the surface is reduced to C_{3v} [15]. Gnezdilov *et al.* [15] reported that the A_{2u}^2 mode at 158 cm^{-1} in the case of Bi_2Se_3 is only observable at temperatures below 10 K for their bulk crystalline sample. In contrast, for our nanoflake samples, we were able to observe this mode even at elevated temperatures up to $\sim 160\text{ K}$ (see Fig. S-9 in the Supplemental Material [32]), indicating enhanced surface contributions with respect to the scattering volume at lower temperatures. Likewise, the IR modes in the Bi_2Te_3 films are detected for temperatures up to 100 K (see Fig. S-9 in the Supplemental Material [32]). Furthermore, the high single crystalline quality of our flakes is indicated by the nearly resolution-limited linewidths of the Bi_2Te_3 phonons. In Sec. 5 in the Supplemental Material [32], we discuss in detail that the narrow linewidths and high quality of the Bi_2Se_3 spectra suggest nearly stoichiometric samples with only a few Se vacancies. Furthermore, a sensitivity of the phonons to band-bending effects due to adsorbates at the surface and consequent localized electronic surface states cannot be seen. Since Raman is a volume scattering technique, we do not expect to observe any contributions from possible highly localized electronic states at the sample surface. This leads us to conclude that the phonons track the CSSs and electronic states associated to the Fermi level of our sample. Furthermore, we conclude from the low number of Se vacancies that the Fermi level in our sample lies indeed between the bulk valence and conduction band.

We conducted a detailed temperature dependent Raman study by acquiring 30 spectra for each material system in a temperature range from 3 to 295 K. To investigate the phonon dynamics, we extracted the values of the frequency ω and the linewidth Γ [full width at half maximum (FWHM)] from the respective Voigt fits to the phonon modes. The Voigt profile is represented by a Lorentz profile broadened by a Gaussian that accounts for the spectral resolution of the spectrometer, and is given as

$$V(\omega) = y_0 + A \frac{2 \ln 2 \Gamma_L}{\pi^{3/2} \Gamma_G^2} \times \int_{-\infty}^{\infty} \frac{e^{-t^2}}{(\sqrt{\ln 2} \frac{\Gamma_L}{\Gamma_G})^2 + (\sqrt{4 \ln 2} \frac{\omega - \omega_0}{\Gamma_G} - t)^2} dt. \quad (1)$$

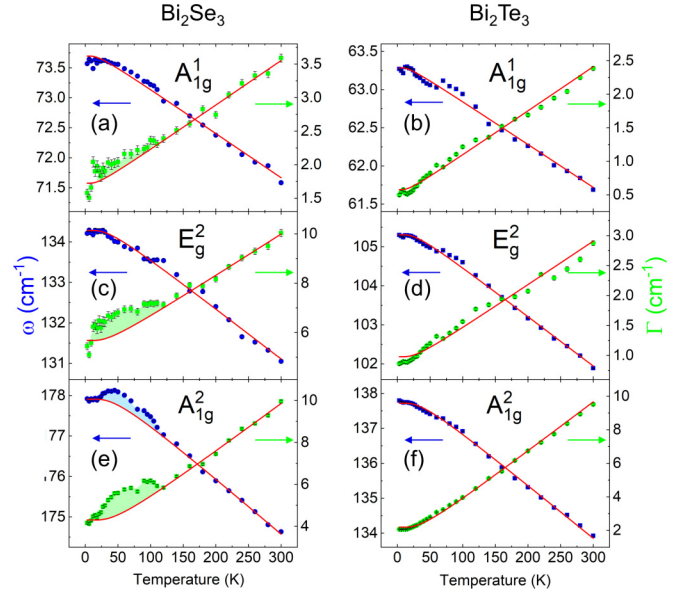


FIG. 2. Self-energy effects from Voigt fits of the temperature dependent Raman response for Bi_2Se_3 (left column) and Bi_2Te_3 (right column). (a),(b) The A_{1g}^1 phonons, (c),(d) the E_g^2 phonons, and (e),(f) the A_{1g}^2 phonons. The red lines are fits using the model of an anharmonic decay with a symmetric decay channel into two acoustic phonons. The data show the general trend of an anharmonic decay consisting of broadening and softening with increasing temperature. Clear deviations from the model are present for the high-energy modes in Bi_2Se_3 [(c) and (e)], which are mirrored in energy and linewidth. Below $\sim 120\text{ K}$, the phonons exhibit higher energies and linewidths than expected from the usual anharmonic phonon decay, as an indication for additional phonon interactions with the electronic system.

Hereby, $\Gamma_{G,L}$ denotes the linewidth of both convoluted peaks, with a spectral resolution of the setup of $\Gamma_G = 1.4\text{ cm}^{-1}$, ω_0 is the peak center, A is the integrated area of the Lorentzian peak, and y_0 is the offset.

We have analyzed the three higher-energy modes of the commonly known [14,39] four bulk modes in Bi_2X_3 ($X = \text{Se}, \text{Te}$) because the lowest-energy E_g^1 mode was covered by the strong Rayleigh background due to the enhanced elastic scattering from the nanoflakes. Figure 2 shows the behavior of the frequency ω_0 and linewidth Γ_L of the A_{1g}^1 , E_g^2 , and A_{1g}^2 modes for Bi_2Se_3 (left column) and Bi_2Te_3 (right column). The frequencies and linewidths show a general trend of phonon softening and broadening with increasing temperature by several wave numbers. This phonon behavior can be described by the model of an anharmonic decay (AD) assuming a symmetric decay of the optical phonon into two acoustic phonons [42]. Within this model, the temperature dependences of the phonon frequency and linewidth are given by

$$\omega_{\text{anh}}(T) = \omega_0 - \frac{a}{e^{\frac{\hbar\omega_0}{2k_B T}} - 1}, \quad (2)$$

$$\Gamma_{\text{anh}}(T) = \Gamma_0 + \frac{a}{e^{\frac{\hbar\omega_0}{2k_B T}} - 1}, \quad (3)$$

with T as the temperature, ω_{anh} and Γ_{anh} as the modulated frequency and linewidth, respectively, and ω_0 and Γ_0 as the bare phonon frequency and linewidth of a particular phonon, respectively. a contains the transition matrix element and the two-phonon density of states of the anharmonic decay. Fits of the data according to the AD model are shown as red lines in Fig. 2. For Bi_2Te_3 , the anharmonic fits show very good agreement with the data, especially for the highest-energy A_{1g}^2 mode in Fig. 2(f). This indicates a more bulklike behavior typical for semiconductors and insulators with phonon-phonon interactions as the dominant scattering mechanism in the Bi_2Te_3 sample. Compared to Bi_2Te_3 , the linewidths for all Raman modes in Bi_2Se_3 show clear deviations from the AD model at temperatures below 120 K; see Figs. 2(a), 2(c) and 2(e). The linewidth of the A_{1g}^1 mode exhibits only weak deviations from the AD model, whereas the higher-energy modes deviate more strongly. For the A_{1g}^2 mode, the deviation in linewidth is mirrored in frequency, illustrated in Fig. 2(e), as expected by the Kramers-Kronig relation. In previous temperature dependent Raman investigations on Bi_2Se_3 crystals [19,20], no phonon anomalies were observed. This hints to an origin of these deviations stemming from the increased electronic surface contributions of the investigated flakes at lower temperatures. This aspect is supported by the enhanced electron density near the Fermi edge in Bi_2Se_3 , shown in Fig. 1(b).

Since the AD model is not sufficient to describe the low-temperature behavior of phonons, additional scattering mechanisms need to be taken into consideration. As Bi_2Se_3 is nonmagnetic, additional scattering channels could stem from electron-phonon interactions since the only available states at these energies and low temperatures must be of an electronic nature. The coupling of phonons to available electronic susceptibilities would result in a decay of the phonons by creating electron-hole pairs [43,44]. The possibility of this interaction is plausible since our XPS data show a higher electron density near the Fermi edge for Bi_2Se_3 . The coupling of phonons to an electric susceptibility $\chi^{\text{el}}(\omega)$ leads to a correction in the phonon self-energy, which manifests itself in a modified Raman response. This response $I^{\text{ph}}(\omega)$ of a phonon coupled to an electric susceptibility $\chi^{\text{el}}(\omega)$,

$$\chi^{\text{el}}(\omega) = R(\omega) + i\rho(\omega), \quad (4)$$

with its real $R(\omega)$ and imaginary part $\rho(\omega)$, is expressed by [45,46]

$$I^{\text{ph}}(\omega) \propto \frac{[g^2\rho(\omega) + \Gamma_{\text{anh}}]\omega_{\text{anh}}}{\underbrace{\left\{\omega^2 - \omega_{\text{anh}}^2 \left[1 - g^2 \frac{R(\omega)}{\omega_{\text{anh}}}\right]\right\}^2}_{\omega_{\text{exp}}^2} + \underbrace{\omega_{\text{anh}}^2 [\Gamma_{\text{anh}} + g^2\rho(\omega)]^2}_{\Gamma_{\text{exp}}^2}}. \quad (5)$$

Here, ω_{anh} and Γ_{anh} correspond to the frequency and linewidth expected from the AD model, and g is a coupling constant determining the coupling strength between the phonon and the electric susceptibility. Equation (5) describes a Lorentz profile with a phonon frequency ω_{anh} that is modified by coupling to the real part $R(\omega)$ of the electric susceptibility and a linewidth Γ_{anh} modified by coupling to the imaginary part $\rho(\omega)$. As a result, the values for the frequency ω_{exp} and

linewidth Γ_{exp} extracted from Voigt fits of the phonons differ from the values expected for an anharmonic decay due to corrections from the electric susceptibility. We hence interpret the deviations in linewidth and frequency expected from the AD model as arising from additional contributions caused by the decay of phonons coupling to an available electronic transition. When the electron-phonon coupling g is strong enough, the extracted phonon linewidths and frequencies are therefore given as follows:

$$\omega_{\text{exp}} = \sqrt{\omega_{\text{anh}}(T)^2 - \omega_{\text{anh}}(T) \cdot g^2 R(\omega)}, \quad (6)$$

$$\Gamma_{\text{exp}} = \Gamma_{\text{anh}}(T) + g^2 \rho(\omega). \quad (7)$$

The deviations from the AD model could be caused by an interaction of the phonons with an electric susceptibility with an energy in the meV range. The lack of any electronic renormalization in Bi_2Te_3 is thus indicating that there are no available electronic states in this energy range. This is further verified by the strongly diminished electronic density near the Fermi edge in Bi_2Te_3 compared to Bi_2Se_3 seen by XPS, as shown in Fig. 1(b).

Since the A_{1g}^2 - and E_g^2 -symmetry phonons show deviations from the AD model, it can be argued that both phonons couple to a close-lying electronic transition. The different energies of the two phonons lead to different corrections from the real and imaginary parts of the electric susceptibility according to Eqs. (6) and (7).

The strong electronic renormalization in Bi_2Se_3 for the E_g^2 mode in linewidth but none in frequency, shown in Fig. 2(c), leads to the assumption that the E_g^2 phonon couples to an electric susceptibility with an energy identical to the E_g^2 energy, as visualized in Fig. 3(a). In that way, the E_g^2 phonon would get a strong correction from the imaginary part $\rho(\omega)$ since it is located at the maximum, resulting in an increased linewidth Γ_{exp} according to Eq. (7). On the other hand, there would not be any corrections in frequency because at ω_{ph} the real part $R(\omega)$ is zero and thus ω_{exp} corresponds to ω_{anh} according to Eq. (6). The temperature dependence of the E_g^2 frequency is then sufficiently well described by the AD model, as evident in Fig. 2(c). Following this hypothesis, the A_{1g}^2 phonon with an energy of 22 meV would couple to $\rho(\omega)$ and a negative $R(\omega)$ of the same electric susceptibility, as illustrated in Fig. 3(b). This would again result in increased linewidths and additionally in increased frequencies according to Eqs. (6) and (7). Our hypothesis agrees well with the observed deviations in frequency and linewidth at lower temperatures for the A_{1g}^2 phonon shown in Fig. 2(e). In this picture, we expect to observe these effects at lower temperatures where phonons are frozen out and the scattering mechanism is dominated by the electron-phonon coupling. This is again in good agreement with our data, where we observe deviations from the AD model setting in at temperatures below 120 K. Heid *et al.* have calculated the coupling strengths of the Bi_2Se_3 CSSs to optical modes as a function of phonon energy [47]. They show that enhanced coupling occurs to phonons within an energy range of 17 to 22 meV with a reduced coupling for modes below 10 meV [47]. Even though Heid *et al.* state that the dominant coupling occurs via polar-type optical modes, significant coupling to Raman-active modes of the electron-

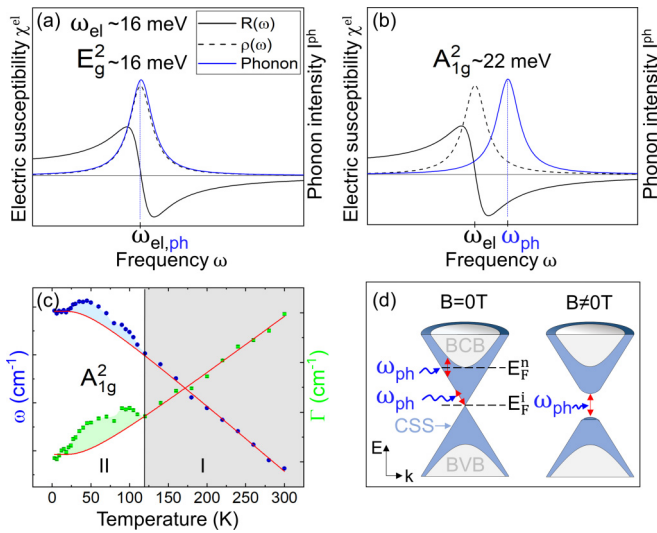


FIG. 3. (a),(b) The real $R(\omega)$ and imaginary $\rho(\omega)$ parts of the electric susceptibility are plotted together with the discrete state of a phonon modeled by a simple Lorentzian with a phonon frequency ω_{ph} . An overlap of both states is shown for the E_g^2 mode in (a) and the A_{1g}^2 mode in (b). (c) Temperature dependence of frequency and linewidth of the Bi_2Se_3 A_{1g}^2 phonon. Two areas are indicated that account for different decay mechanisms of the phonon. (d) Schematic band structure of Bi_2Se_3 with two possible locations of the Fermi level in an intrinsic (E_F^i) and n -doped (E_F^n) Bi_2Se_3 nanoflake. The bulk conduction band (BCB) and bulk valence band (BVB) are labeled. Red arrows illustrate creations of electron-hole pairs by a Raman phonon ω_{ph} . The gapped Dirac cone is shown when a magnetic field $B \neq 0$ T is applied.

phonon interaction is still present, as suggested in several studies [11,48]. Thus, our observations are in good agreement with the calculated coupling strengths, which support our findings for only very weak renormalizations in the A_{1g}^1 mode at 9 meV and strong renormalizations in the E_g^2 (16.7 meV) and A_{1g}^2 (21.9 meV) modes. The preceding analysis leads to the identification of two temperature regions with different dominant scattering mechanisms that are shown in Fig. 3(c). In region I, at higher temperatures, phonon-phonon coupling dominates the phonon decay by the anharmonic interaction and additional contributions from electron-phonon coupling are no longer evident. Therefore, we observe good agreement with the classic AD model in region I, where the bulk properties mask all surface-related effects. In region II, electron-phonon coupling is significant and phonon renormalization can be observed when the surface contribution is high enough.

So far, we discussed the electron-phonon coupling from an energetic point of view. The A_{1g}^1 phonon with an energy of around 9 meV should interfere with the electric susceptibility around 16 meV by coupling to the positive imaginary and real part. However, we do not observe electronic renormalizations for this mode. Hence, an additional aspect has to be considered that affects the coupling strength g between the phonons and the electric susceptibility. The eigenvectors of the phonons show significantly different displacement vectors for the A_{1g}^1 phonon compared to the E_g^2 and A_{1g}^2 phonons.

The atomic displacements for the E_g^2 and A_{1g}^2 modes modulate the electric susceptibility related to the CSSs in the following way: For both modes, the partially negatively charged chalcogen (Se, Te) atoms terminating each QL vibrate opposite to the positively charged Bi atoms [18,49], whereas they vibrate in phase for the A_{1g}^1 mode. The electronic polarizability is, therefore, affected more strongly by the E_g^2 and A_{1g}^2 phonons, resulting in a stronger electron-phonon coupling and enhanced self-energy effects.

In a perfect single-crystalline Bi_2Se_3 sample the Fermi level is expected to be located at the Dirac point [7], as indicated in Fig. 3(d). In this case, intracone electronic transitions in the upper Dirac cone are available. The electron-phonon coupling strength increases linearly with the energy distance from the Dirac point due to the linear increase of the density of states expected for the 2D Dirac dispersion [47]. It is also possible that the Fermi level lies closer to the bulk conduction band due to inherent n doping that is often reported for naturally grown Bi_2Se_3 [33] and is also shown in Fig. 3(d). In that case, transitions of the Dirac fermions into the bulk conduction band become possible and add to the intracone contributions. The coupling strength is expected to be enhanced when additional interband transitions are available [47], which explains our observed strong phonon renormalizations. We, therefore, expect the Fermi level in our Bi_2Se_3 samples to lie within the bulk gap but closer to the bulk conduction bands.

The assumption of χ^{el} being related to the CSSs is justified by two aspects. First, we were able to show the enhanced surface contributions of our flakes by the detection of IR modes up to high temperatures. Second, the electric susceptibility in the meV range can be associated with transitions involving Dirac cone states. Additional insight can be gained by manipulating the Dirac cone and the associated electric susceptibility by means of a magnetic field. Since the Dirac cone determines the low-energy electric susceptibility, its modification is also indicative of the presence of the CSSs. The changes in frequency and linewidth of the phonons as a function of magnetic field for Bi_2Se_3 and Bi_2Te_3 are shown in Figs. 4(a) to 4(f).

In agreement with our temperature dependent study and XPS results, we observe a magnetic field dependent renormalization of phonon energies and linewidths in Bi_2Se_3 , but not in Bi_2Te_3 . The absence of any phonon renormalization in Bi_2Te_3 is again consistent with the reduced electronic density near the Fermi edge compared to the Bi_2Se_3 sample. For Bi_2Se_3 , however, magnetic field dependent self-energy corrections are observed in frequency and linewidth for the A_{1g}^2 mode at 177 cm^{-1} . At fields above 3 T, we find a simultaneous hardening and broadening of about 0.6 cm^{-1} and 1.5 cm^{-1} , respectively. Since it is known that in topological insulators a gap opening in the Dirac cone occurs in the presence of a magnetic field [23], our results point to a change in the electric susceptibility of the Dirac cone by the magnetic field. The change in the electric susceptibility would lead to a renormalization in the A_{1g}^2 mode in Bi_2Se_3 . A gap opening would shift and redistribute the electric susceptibility. The hardening and broadening of the A_{1g}^2 mode with increasing field strengths indicate the coupling to an electric

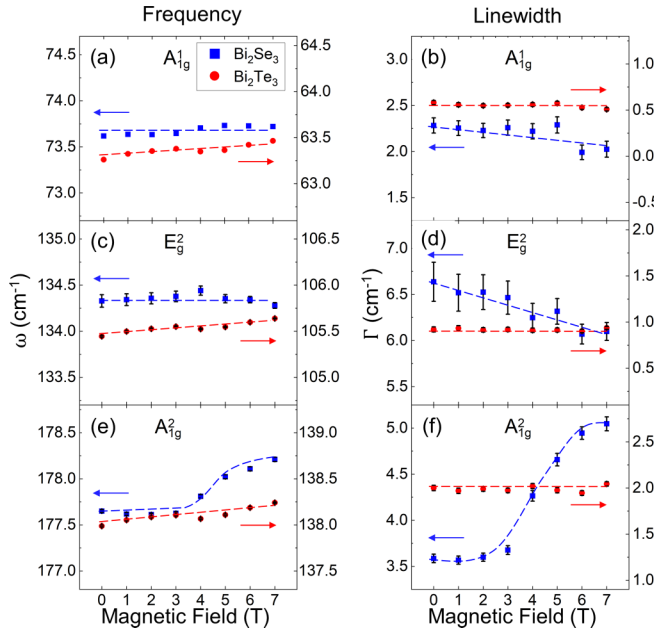


FIG. 4. Magnetic field dependent self-energy effects for Bi_2Se_3 and Bi_2Te_3 nanoflakes at 3 K in (X -)scattering geometry and Faraday configuration. The dependency of the three Raman modes in energy (left column) and linewidth (right column) with magnetic field is shown. All y axes are set to intervals of 2.0 cm^{-1} for easier comparability. Bi_2Te_3 phonons (red curves) show no significant change in energy and linewidth over the applied magnetic field range. For the Bi_2Se_3 phonons (blue curves), clear changes in energy and linewidth can be observed for magnetic fields above 3 T. The dashed lines represent guides to the eye.

susceptibility with a lower energy than the phonon according to Eqs. (6) and (7). The decreasing linewidth of the E_g^2 mode, on the other hand, shows a reduced coupling to the electric susceptibility. We can therefore estimate the energy of a gap opening in the Dirac cone to be in the range of 16 to 22 meV, which would explain the phonon renormalizations. This finding is in agreement with results of Gooth *et al.* [50], who report a gap opening in the order of tens of meV by magnetic interactions in TI. According to our model, the phonons decay by coupling to interband transitions from the lower gapped Dirac cone to the upper one, as visualized in Fig. 3(d). The strong phonon self-energy corrections due to the electron-phonon interactions provide direct evidence

for the changes in the electric susceptibility in the CSSs at magnetic field strengths above 3 T.

IV. CONCLUSION

In conclusion, we have investigated thin films of drop-casted Bi_2Se_3 and Bi_2Te_3 nanoflakes by means of temperature and magnetic field dependent Raman spectroscopy. The temperature dependence of the phonon dynamics in our Bi_2Te_3 sample is readily described by the anharmonic phonon-phonon interaction, indicating a dominant bulk behavior. For Bi_2Se_3 , we observe deviations from the AD model, which can be linked to additional contributions from the electron-phonon interaction originating from the increased surface contribution. Our study suggests that the Dirac fermions contribute significantly to the electron-phonon interactions, which manifest in the strong phonon renormalizations in Bi_2Se_3 at temperatures below 120 K. Additional magnetic field dependent Raman spectroscopy reveals strong phonon self-energy corrections in Bi_2Se_3 , indicating the renormalization of the phonons by the continuum free carriers and a significant magnetoelectric coupling. The self-energy changes in the Bi_2Se_3 phonons provide direct evidence for the manipulation of the CSSs by an applied magnetic field, which can be associated with a gap opening in the Dirac cone.

ACKNOWLEDGMENTS

This work was funded by the Deutsche Forschungsgemeinschaft (DFG; German Research Foundation), DFG RU 773/8-1. Work at the University of Illinois was supported by the National Science Foundation under Grant No. NSF DMR 1800982. S.B., C.U., and M.R. would like to acknowledge the support from the Australian Research Council (ARC) through Grant No. DP170100415. The work at National University of Singapore is supported by the Ministry of Education of Singapore AcRF Tier-2 (Grants No. MOE2017-T2-1-135, No. 323 MOE2018-T2-2-117, and No. MOE2018-T2-2-117), and Ministry of Education AcRF-1 (Grant No. R-144-000-423-114) and is acknowledged by the support of the Singapore Synchrotron Light Source (SSLS), which is a National Research Infrastructure under the National Research Foundation Singapore via NUS Core Support Grant No. C-380-003-003-001. We thank Robert Frömter and Dorota Koziej for the use of their scanning electron microscopes. We are further thankful for Robert Zierold and Stephan Martens for helpful discussions and magnetization measurements of our samples.

- [1] M. Z. Hasan and C. L. Kane, *Colloquium: Topological insulators*, *Rev. Mod. Phys.* **82**, 3045 (2010).
- [2] K. Von Klitzing, The quantized Hall effect, *Rev. Mod. Phys.* **58**, 519 (1986).
- [3] L. Fu, C. L. Kane, and E. J. Mele, Topological Insulators in Three Dimensions, *Phys. Rev. Lett.* **98**, 106803 (2007).
- [4] J. Betancourt, S. Li, X. Dang, J. Burton, E. Tsybal, and J. Velez, Complex band structure of topological insulator Bi_2Se_3 , *J. Phys.: Condens. Matter* **28**, 395501 (2016).

- [5] Y. Ando, Topological insulator materials, *J. Phys. Soc. Jpn.* **82**, 102001 (2013).
- [6] J. G. Analytis, J.-H. Chu, Y. Chen, F. Corredor, R. D. McDonald, Z. X. Shen, and I. R. Fisher, Bulk Fermi surface coexistence with Dirac surface state in Bi_2Se_3 : A comparison of photoemission and Shubnikov–de Haas measurements, *Phys. Rev. B* **81**, 205407 (2010).
- [7] H. Zhang, C.-X. Liu, X.-L. Qi, X. Dai, Z. Fang, and S.-C. Zhang, Topological insulators in Bi_2Se_3 , Bi_2Te_3 and Sb_2Te_3

- with a single Dirac cone on the surface, *Nat. Phys.* **5**, 438 (2009).
- [8] Y. Xia, D. Qian, D. Hsieh, L. Wray, A. Pal, H. Lin, A. Bansil, D. Grauer, Y. S. Hor, R. J. Cava, and M. Z. Hasan, Observation of a large-gap topological-insulator class with a single Dirac cone on the surface, *Nat. Phys.* **5**, 398 (2009).
- [9] Y. L. Chen, J. G. Analytis, J.-H. Chu, Z. K. Liu, S.-K. Mo, X. L. Qi, H. J. Zhang, D. H. Lu, X. Dai, Z. Fang, S. C. Zhang, I. R. Fisher, Z. Hussain, and Z.-X. Shen, Experimental realization of a three-dimensional topological insulator, Bi_2Te_3 , *Science* **325**, 178 (2009).
- [10] D. Kim, Q. Li, P. Syers, N. P. Butch, J. Paglione, S. D. Sarma, and M. S. Fuhrer, Intrinsic Electron-Phonon Resistivity of Bi_2Se_3 in the Topological Regime, *Phys. Rev. Lett.* **109**, 166801 (2012).
- [11] C. Chen, Z. Xie, Y. Feng, H. Yi, A. Liang, S. He, D. Mou, J. He, Y. Peng, X. Liu *et al.*, Tunable Dirac fermion dynamics in topological insulators, *Sci. Rep.* **3**, 2411 (2013).
- [12] M. Eddrief, P. Atkinson, V. Etgens, and B. Jusserand, Low-temperature Raman fingerprints for few-quintuple layer topological insulator Bi_2Se_3 films epitaxied on GaAs, *Nanotechnology* **25**, 245701 (2014).
- [13] S. Zhao, C. Beekman, L. Sandilands, J. Bashucky, D. Kwok, N. Lee, A. LaForge, S.-W. Cheong, and K. Burch, Fabrication and characterization of topological insulator Bi_2Se_3 nanocrystals, *Appl. Phys. Lett.* **98**, 141911 (2011).
- [14] K. Shahil, M. Hossain, V. Goyal, and A. Balandin, Micro-Raman spectroscopy of mechanically exfoliated few-quintuple layers of Bi_2Te_3 , Bi_2Se_3 , and Sb_2Te_3 materials, *J. Appl. Phys.* **111**, 054305 (2012).
- [15] V. Gnezdilov, Y. G. Pashkevich, H. Berger, E. Pomjakushina, K. Conder, and P. Lemmens, Helical fluctuations in the Raman response of the topological insulator Bi_2Se_3 , *Phys. Rev. B* **84**, 195118 (2011).
- [16] D. Teweldebrhan, V. Goyal, and A. A. Balandin, Exfoliation and characterization of bismuth telluride atomic quintuples and quasi-two-dimensional crystals, *Nano Lett.* **10**, 1209 (2010).
- [17] K. M. F. Shahil, M. Hossain, D. Teweldebrhan, and A. Balandin, Crystal symmetry breaking in few-quintuple Bi_2Te_3 films: Applications in nanometrology of topological insulators, *Appl. Phys. Lett.* **96**, 153103 (2010).
- [18] W. Richter, C. R. Becker, and H. Köhler, A Raman and far-infrared investigation of phonons in the rhombohedral $\text{V}_2\text{-VI}_3$ compounds, *Phys. Status Solidi (b)* **84**, 619 (1977).
- [19] B. Irfan, S. Sahoo, A. P. S. Gaur, M. Ahmadi, M. J.-F. Guinel, R. S. Katiyar, and R. Chatterjee, Temperature dependent Raman scattering studies of three dimensional topological insulators Bi_2Se_3 , *J. Appl. Phys.* **115**, 173506 (2014).
- [20] Y. Kim, X. Chen, Z. Wang, J. Shi, I. Miotkowski, Y. P. Chen, P. A. Sharma, A. L. Lima Sharma, M. A. Hekmaty, Z. Jiang, and D. Smirnov, Temperature dependence of Raman-active optical phonons in Bi_2Se_3 and Sb_2Te_3 , *Appl. Phys. Lett.* **100**, 071907 (2012).
- [21] F. Zhou, Y. Zhao, W. Zhou, and D. Tang, Temperature-dependent Raman scattering of large size hexagonal Bi_2Se_3 single-crystal nanoplates, *Appl. Sci.* **8**, 1794 (2018).
- [22] D. Li, L. Li, D.-W. Liu, and J.-F. Li, Temperature dependence of the Raman spectra of Bi_2Te_3 and $\text{Bi}_{0.5}\text{Sb}_{1.5}\text{Te}_3$ thermoelectric films, *Phys. Status Solidi RRL* **6**, 268 (2012).
- [23] X.-L. Qi, T. L. Hughes, and S.-C. Zhang, Topological field theory of time-reversal invariant insulators, *Phys. Rev. B* **78**, 195424 (2008).
- [24] Y. Chen, J.-H. Chu, J. Analytis, Z. Liu, K. Igarashi, H.-H. Kuo, X. Qi, S.-K. Mo, R. Moore, D. Lu *et al.*, Massive Dirac fermion on the surface of a magnetically doped topological insulator, *Science* **329**, 659 (2010).
- [25] P. Sessi, R. R. Biswas, T. Bathon, O. Storz, S. Wilfert, A. Barla, K. A. Kokh, O. E. Tereshchenko, K. Fauth, M. Bode *et al.*, Dual nature of magnetic dopants and competing trends in topological insulators, *Nat. Commun.* **7**, 12027 (2016).
- [26] W. Luo and X.-L. Qi, Massive Dirac surface states in topological insulator/magnetic insulator heterostructures, *Phys. Rev. B* **87**, 085431 (2013).
- [27] P. Wei, F. Katmis, B. A. Assaf, H. Steinberg, P. Jarillo-Herrero, D. Heiman, and J. S. Moodera, Exchange-Coupling-Induced Symmetry Breaking in Topological Insulators, *Phys. Rev. Lett.* **110**, 186807 (2013).
- [28] S. Buchenau, P. Sergelius, C. Wiegand, R. Zierold, H. S. Shin, M. Rübhausen, J. Gooth, K. Nielsch *et al.*, Symmetry breaking of the surface mediated quantum Hall effect in Bi_2Se_3 nanoplates using Fe_3O_4 substrates, *2D Mater.* **4**, 015044 (2017).
- [29] D. Biswas, S. Thakur, K. Ali, G. Balakrishnan, and K. Maiti, Anomalies of a topologically ordered surface, *Sci. Rep.* **5**, 10260 (2015).
- [30] S. Buchenau, L. O. Akinsinde, M. Zocher, D. Rukser, U. Schürmann, L. Kienle, B. Grimm-Lebsanft, and M. Rübhausen, Scalable polyol synthesis for few quintuple layer thin and ultra high aspect ratio Bi_2Se_3 structures, *Solid State Commun.* **281**, 49 (2018).
- [31] Y. Zhang, L. P. Hu, T. J. Zhu, J. Xie, and X. B. Zhao, High yield Bi_2Te_3 single crystal nanosheets with uniform morphology via a solvothermal synthesis, *Crystal Growth Des.* **13**, 645 (2013).
- [32] See Supplemental Material at <http://link.aps.org/supplemental/10.1103/PhysRevB.101.245431> for details of the nanoflake synthesis and characterization, additional Raman measurements, and *n*-doping study of the Bi_2Se_3 nanoflakes.
- [33] Y. Zhang, K. He, C.-Z. Chang, C.-L. Song, L.-L. Wang, X. Chen, J.-F. Jia, Z. Fang, X. Dai, W.-Y. Shan, S.-Q. Shen, Q. Niu, X.-L. Qi, S.-C. Zhang, X.-C. Ma, and Q.-K. Xue, Crossover of the three-dimensional topological insulator Bi_2Se_3 to the two-dimensional limit, *Nat. Phys.* **6**, 584 (2010).
- [34] H. M. Benia, C. Lin, K. Kern, and C. R. Ast, Reactive Chemical Doping of the Bi_2Se_3 Topological Insulator, *Phys. Rev. Lett.* **107**, 177602 (2011).
- [35] D. Kong, J. J. Cha, K. Lai, H. Peng, J. G. Analytis, S. Meister, Y. Chen, H.-J. Zhang, I. R. Fisher, Z.-X. Shen *et al.*, Rapid surface oxidation as a source of surface degradation factor for Bi_2Se_3 , *ACS Nano* **5**, 4698 (2011).
- [36] B. Yan, D. Zhang, and C. Felser, Topological surface states of Bi_2Se_3 coexisting with Se vacancies, *Phys. Status Solidi RRL* **7**, 148 (2013).
- [37] B. Schulz, J. Bäckström, D. Budelmann, R. Maeser, M. Rübhausen, M. V. Klein, E. Schoeffel, A. Mihill, and S. Yoon, Fully reflective deep ultraviolet to near infrared spectrometer and entrance optics for resonance Raman spectroscopy, *Rev. Sci. Instrum.* **76**, 073107 (2005).

- [38] C. Arguello, D. L. Rousseau, and S. P. d. S. Porto, First-order Raman effect in wurtzite-type crystals, *Phys. Rev.* **181**, 1351 (1969).
- [39] J. Zhang, Z. Peng, A. Soni, Y. Zhao, Y. Xiong, B. Peng, J. Wang, M. S. Dresselhaus, and Q. Xiong, Raman spectroscopy of few-quintuple layer topological insulator Bi_2Se_3 nanoplatelets, *Nano Lett.* **11**, 2407 (2011).
- [40] Y. Liang, W. Wang, B. Zeng, G. Zhang, J. Huang, J. Li, T. Li, Y. Song, and X. Zhang, Raman scattering investigation of Bi_2Te_3 hexagonal nanoplates prepared by a solvothermal process in the absence of naoh, *J. Alloys Compd.* **509**, 5147 (2011).
- [41] R. He, Z. Wang, R. L. J. Qiu, C. Delaney, B. Beck, T. E. Kidd, C. C. Chancey, and X. P. A. Gao, Observation of infrared-active modes in Raman scattering from topological insulator nanoplates, *Nanotechnology* **23**, 455703 (2012).
- [42] P. G. Klemens, Anharmonic decay of optical phonons, *Phys. Rev.* **148**, 845 (1966).
- [43] N. Bonini, M. Lazzeri, N. Marzari, and F. Mauri, Phonon Anharmonicities in Graphite and Graphene, *Phys. Rev. Lett.* **99**, 176802 (2007).
- [44] E. H. Hasdeo, A. R. T. Nugraha, M. S. Dresselhaus, and R. Saito, Breit-Wigner-Fano line shapes in Raman spectra of graphene, *Phys. Rev. B* **90**, 245140 (2014).
- [45] M. A. Rübhausen, Electronic correlations in cuprate superconductors - An inelastic light scattering study, Ph.D. thesis, Universität Hamburg, 1998.
- [46] M. Cardona, *Light Scattering in Solids I - Introductory Concepts*, edited by M. Cardona (Springer-Verlag, Berlin, 1983).
- [47] R. Heid, I. Yu. Sklyadneva, and E. V. Chulkov, Electron-phonon coupling in topological surface states: The role of polar optical modes, *Sci. Rep.* **7**, 1095 (2017).
- [48] T. Kondo, Y. Nakashima, Y. Ota, Y. Ishida, W. Malaeb, K. Okazaki, S. Shin, M. Kriener, S. Sasaki, K. Segawa *et al.*, Anomalous Dressing of Dirac Fermions in the Topological Surface State of Bi_2Se_3 , Bi_2Te_3 , and Cu-Doped Bi_2Se_3 , *Phys. Rev. Lett.* **110**, 217601 (2013).
- [49] S. Mishra, S. Satpathy, and O. Jepsen, Electronic structure and thermoelectric properties of bismuth telluride and bismuth selenide, *J. Phys.: Condens. Matter* **9**, 461 (1997).
- [50] J. Gooth, R. Zierold, P. Sergelius, B. Hamdou, J. Garcia, C. Damm, B. Rellinghaus, H. J. Pettersson, A. Pertsova, C. Canali *et al.*, Local magnetic suppression of topological surface states in Bi_2Te_3 nanowires, *ACS Nano* **10**, 7180 (2016).